RESEARCH (LIGHT BLUE)

Superior high-temperature mechanical properties and microstructural features of LPBF-printed In625-based metal matrix composites

Emre Tekoglu [a,1], Jong-Soo Bae [b,1], Ho-A Kim [c,1], Kwang-Hyeok Lim [b], Jian Liu [e], Tyler D. Doležal [f,l], So Yeon Kim [a,f], Mohammed A. Alrizqi [a,g], Aubrey Penn [h], Wen Chen [e], A. John Hart [i], Joo-Hee Kang [j], Chang-Seok Oh [j], Jiwon Park [j], Fan Sun [k], Sangtae Kim [c,d,*], Gi-Dong Sim [b,*], Ju Li [a,f,*]

[a] Department of Nuclear Science and Engineering, Massachusetts Institute of Technology, Cambridge, MA 02139, United States
[b] Department of Mechanical Engineering, Korea Advanced Institute of Science and Technology, 291 Daehak-ro, Daejeon, Yuseong-gu 34141, Republic of Korea
[c] Department of Nuclear Engineering, Hanyang University, 222 Wangsimni-ro, Seongdong-gu, Seoul 04763, Republic of Korea
[d] Department of Materials Science and Engineering, Hanyang University, 222 Wangsimni-ro, Seongdong-gu, Seoul 04763, Republic of Korea
[e] Department of Mechanical and Industrial Engineering, University of Massachusetts, Amherst 01003, United States
[f] Department of Materials Science and Engineering, Massachusetts Institute of Technology, Cambridge 02129, United States
[g] School of Mechanical and Aerospace Engineering, Cornell University, Ithaca, NY 14853, United States
[h] MIT.nano, Massachusetts Institute of Technology, Cambridge, MA 02139, United States
[i] Department of Mechanical Engineering, Massachusetts Institute of Technology, Cambridge, MA 02139, United States
[j] Department of Materials Analysis, Korea Institute of Materials Science, 797, Changwondaero, Seongsan-gu, Changwon 51508, Gyeongnam, Republic of Korea
[k] PSL University, Chimie ParisTech, CNRS, Institut de Recherche de Chimie Paris, Paris 75005, France
[l] Department of Engineering Physics, Air Force Institute of Technology, 2950 Hobson Way, Wright-Patterson Air Force Base, OH 45433, United States

The growing demands for high-temperature materials, especially in aerospace and energy production, compel thorough explorations of innovative materials. Here, we demonstrate significantly enhanced high-temperature mechanical properties of Inconel 625 (In625) based metal matrix composites (MMCs) fabricated by laser powder bed fusion (LPBF) additive manufacturing. The MMC feedstocks for LPBF were fabricated with fine ceramic particles (i.e., titanium diboride (TiB_2), titanium carbide (TiC), zirconium diboride (ZrB_2) and zirconium carbide (ZrC)) separately mixed with In625 powders. Among the printed specimens, the In625 + TiB_2 showed an exceptional strength-ductility combination at 800 °C as well as an outstanding creep resistance at 800 °C under 150 MPa tensile stress. The detailed microstructural characterization, along with thermodynamic calculation and atomic simulations, reveal that the addition of TiB_2 results in the formation of serrated grain boundaries, (Cr, Mo)-boride phases near the grain boundaries, and nano-dispersed (Ti, Al, Nb)-oxide phases within the matrix. These features effectively suppress the formation of detrimental high-temperature phases and enhance the material's high-temperature properties. Beyond amplifying the inherent thermal attributes of

RESEARCH (LIGHT BLUE)

In625 superalloy, the research highlights the transformative potential of boride doping and the composition design of MMCs specifically for the LPBF process.

Introduction

High-temperature environments present unique challenges across multiple industries from aerospace to energy production. Whether for designing next-generation jet engines or advanced power plants, the scientific community finds itself navigating the intricacies of material science to discover new material compositions, such as precipitation-strengthened superalloys, high-entropy alloys (HEAs) [1–5] and refractory metals (i.e., niobium, tungsten, molybdenum) [5–9]. Laser powder bed fusion (LPBF) is an additive manufacturing technique that has gained significant attention in recent years for its ability to form complex-geometry and high-performance material components. In LPBF, a high-powered laser selectively melts and fuses powders layer by layer to create a solid object [3,10]. This method allows for the precise control of microstructures and properties, making it ideal for producing parts that can withstand extreme conditions, such as high temperatures, stresses, and corrosive fluids [5,11]. Accordingly, the study at hand focuses on such a pursuit: exploring the high-temperature mechanical characteristics of laser powder bed fusion (LPBF) fabricated Inconel 625 (In625) metal matrix composites (MMCs).

Inconel alloys, encompassing compositions like Inconel 718 (with iron and niobium), and Inconel 939 (with cobalt and titanium), are celebrated for their mechanical properties at high temperatures. Among them, In625 distinguishes itself with its notable strength and resistance to oxidation and corrosion at elevated temperatures [12–14]. Traditionally, In625 has been employed in applications from aerospace components, where high strength-to-weight ratios are paramount, to the aggressive corrosive environments of chemical processing plants. Yet, like all materials, In625 has its limits. With increasing temperatures, In625 suffers from significantly weakened tensile strength above 700 °C due to the limitation of work hardening capabilities, emphasizing the need for reinforcements or modifications to enhance its high-temperature performance [15,16].

Transition-metal borides and carbides, with their impressive hardness and chemical stability, emerge as promising candidates to enhance In625′s high-temperature properties [17–19]. However, seamlessly integrating a reinforcing agent into a base material presents challenges that are often exacerbated by traditional production methods. Many conventional techniques, such as casting or powder metallurgy, struggle with achieving uniform distribution of the reinforcing agent within the base matrix [20,21]. Uneven dispersion can lead to regions of inconsistency, undermining the overall performance of the composite. Additionally, the inadequate interfacial bonding between the base material and the reinforcing agent can deteriorate the transfer of load between the matrix and the reinforcements, diminishing the desired strengthening effect [22]. The production technique is thus of paramount importance as it directly influences the microstructure and, by extension, the overall characteristics of the material.

Within this context, additive manufacturing (AM) comes into play in the fabrication of Inconel-based metal matrix composites (MMCs) [11,17–19,23,24]. By melting powders layer by layer with focused laser beam, LPBF facilitates a controlled, uniform processing, which is essential for achieving the desired properties in MMC [25–27]. In the context of this study, LPBF's capabilities enable the integration of different reinforcing particles within the In625 matrix, potentially overcoming the challenges faced with traditional methods and setting the stage for superior high-temperature properties.

While some studies have delved deep into the creep behavior of In625 [28,29], the introduction of LPBF presents a renewed set of challenges and opportunities [16,30,31]. There is a scarcity of high-temperature creep studies on In625, especially lacking documentation above 800 °C. Based on the surveyed literature, wrought In625 exhibits approximately 50 % creep rupture ductility [29,32]. However, additively manufactured (AM) In625, such as with the LPBF method, displays less than 15 % ductility above 800 °C [30,31]. Incorporating ceramic particles may well aggravate the reduced ductility. Yet in our previous study, we showed that AM In718 + ZrB$_2$ has an exceptional tensile ductility (10 times that of pure In718) with 10 % higher yield strength (σ_{YS}) and 8 % higher ultimate tensile strength (σ_{UTS}) than pure In718 at 800 °C [25]. It was suggested that the zirconium diboride (ZrB$_2$) addition into In718 not only promotes grain boundary serration but also reduces the as-printed porosity [25]. While transition metal borides and carbides should promote strength as ceramic strengtheners, their interactions with In625, especially under the LPBF process, remain an area ripe for explorations in terms of the strength/ductility trade-off and high-temperature creep performance.

This work employs a two-fold approach: LPBF process to compare the high-temperature tensile properties of In625 MMCs fortified with 2 wt% ceramic particles of different types including TiB$_2$, TiC, ZrB$_2$, and ZrC, followed by an in-depth assessment of the creep behaviors at 800 °C of these composites. Improving the creep rupture resistance of In625, particularly through synergistic integration with TiB$_2$ via LPBF, demonstrates significant promise for its utilization as an engineering material in high-temperature applications. Furthermore, these findings could catalyze further research, setting the stage for the development of ductile MMCs tailored for specific high-temperature challenges.

Material and methods
Feedstock preparation
In this study, In625 powders were provided by MSE Supplies LLC, Tuczon, AZ, USA. The SEM images of these powders are shown in Supplementary Fig. 1, revealing a particle size distribu-

tion between 15 to 45 μm. TiB_2, ZrB_2, TiC, and ZrC powders with an average diameter below 2 μm were procured from US Research Nanomaterials Inc. The scanning electron microscopy (SEM) images of these powders (Supplementary Fig. 1) confirm their size distribution not exceeding 2 μm. The ceramic powders were blended with In625 to achieve a composition with 2 wt% TiB_2, ZrB_2, TiC and ZrC, separately. A batch blend of 500 g was subjected to a high-speed blender (VM0104, Vita-Mix, USA) for an uninterrupted duration of 90 min.

LPBF process parameter
The as-received In625 powders and the composite powders mixed with 2 wt% TiB_2, ZrB_2, TiC, and ZrC through blade mixing were all subjected to LPBF using an EOS M290 system. The LPBF parameters used in this study are shown in Supplementary Table 1. These parameters were employed for both the unmodified In625 and the composite powders.

Materials characterization
Samples were first sectioned, ground and polished in preparation for SEM characterization. The Zeiss Merlin high-precision SEM (Carl Zeiss AG, Germany) was used for the assessment of microstructural features and elemental distribution. The same SEM facilitated Electron backscatter diffraction (EBSD) studies. For transmission electron microscopy (TEM) sample preparation, a Zeiss Vision 40 CrossBeam focused ion beam (FIB) was employed. Post-FIB, scanning transmission electron microscopy (STEM) imaging and spectroscopy were conducted using a JEOL 2010F field emission STEM (from JEOL Ltd., Japan) operating at 200 kV. Additional STEM imaging, energy dispersive X-ray spectroscopy (EDS), and electron energy-loss spectroscopy (EELS) were performed using a probe-corrected Thermo Fisher Themis Z G3 equipped with Super-X detectors and a Gatan Contiuum EELS spectrometer. Images and spectra were collected with a convergence angle of 19 mrad and probe current of 200 pA. The Zeiss Xradia 620 Versa X-ray microscope was used to perform computed tomography (CT) to measure the porosity distribution and size in the printed samples. A pixel size of 1.75 μm, filter of HE18, beam energy of 160 keV, a power of 25 W, exposure time of 5 s, and full 360° rotation were used for 4X scans of the 3D printed specimen. Dragonfly software was used for post-processing of the data, where the pores lower than 9 voxel size (i.e., pores below 1.75 μm) were removed. Room-temperature tensile tests were performed using the Instron 5969 at a strain rate of 2×10^{-4} s^{-1}. A non-contacting AVE2 video extensometer precisely recorded the tensile displacement and strain. Tensile tests at 800 °C, with the same strain rate, were conducted in a custom-built tensile testing rig, inclusive of a 1000 °C capable furnace (Supplementary Fig. 2(a)). This setup consists of a linear actuator (Physik Instrument (PI) GmbH & Co.), load cell (FUTEK Advanced Sensor Technology, Inc.), and an XYZ linear stage. Strain readings in the gauge section were measured through the digital image correlation (DIC) method. For stable DIC strain measurement at elevated temperatures, white aluminum oxide aerosol paint and black heat-resistant paint were sprayed on the gauge section of each specimen to create high-contrast speckle patterns. Sample images were captured every 2 s during the test using a charge-coupled device (CCD) camera (Teledyne

FLIR, Inc.) with a telecentric lens (Edmund Optics, Inc.). Creep tests were conducted at 800 °C and 150 MPa using a customized creep test equipment (Supplementary Fig. 2(b)). The equipment comprises a furnace capable of heating up to 1200 °C, a linear variable displacement transducer (LVDT) for measuring specimen displacement, a loading system for applying a constant load on the specimen, a load cell for load measurement, and a controller capable of overall temperature and load control. The experimental procedure involves heating up to the experimental temperature of 800 °C at a heating rate of 10 °C/min, followed by a 60-minute temperature stabilization period at 800 °C. A stress of 150 MPa was then applied to the specimen (Supplementary Fig. 2(c)). Following specimen failure in the creep tests, the system was promptly shut down, naturally cooling the specimen inside the furnace. Schematic representations of the room temperature (RT) and high-temperature tensile and creep test samples, along with their dimensions, are provided in Supplementary Fig. 2(d). Atom probe tomography (APT) analysis evaluated atomic segregation within the In625 + TiB_2 specimen. APT tips were fabricated using FIB milling from the identified GB area (Supplementary Fig. 3). Calculations of Phase Diagram (CALPHAD) simulation was calculated based on ThermoCalc ver. 2023b with ThermoTech TTNI8 database (Supplementary Table 2).

Results and discussion
The SEM image and corresponding EDX mapping signals presented in Fig. 1(a) reveal the maintenance of the spherical morphology of In625 particles, even after blending with TiB_2. Furthermore, EDX signals obtained from Ti and B elements reveal the decoration of TiB_2 powders on the In625 particles, highlighting the effective blending of these two materials without sacrificing the overall sphericity of the In625 particles. High-magnification SEM images and the corresponding EDX mapping analysis of all the composite powders (i.e., In625 + TiB_2, In625 + TiC, In625 + ZrB_2, and In625 + ZrC) are presented in Supplementary Fig. 4. It is noteworthy that all the composite powders preserved their spherical morphology as well as effective decoration of ceramic nanoparticles onto the In625 particulate surface after the blending. Lastly, there is a marked contrast between the surface morphology of the pure In625 particles (Supplementary Fig. 1) and its composite counterparts (Supplementary Fig. 4), further confirming the nanoparticle-decorated In625 particle surfaces as opposed to un-decorated pure In625 particles.

After blending, the powders underwent the LPBF (Fig. 1(b)). The 3D CT reconstructions of the as-printed In625 and In625 + TiB_2 shown in Fig. 1(c, d) exhibit a nearly full density range in both materials (>99.8 %). While In625 + TiB_2 displays a slightly reduced mean pore size (23.3 μm) compared to pure In625 (30.4 μm) (Supplementary Fig. 5), both materials predominantly exhibit spherical pores (sphericity > 0.9), indicating that porosities resulted from entrapped gas rather than insufficient fusion (Supplementary Fig. 5). Cross-sectional SEM images presented in Fig. 1(e, f) highlight the gas porosities (indicated by white arrows) in In625 and In625 + TiB_2 samples. However, besides the similarity in pore morphology, remarkable differ-
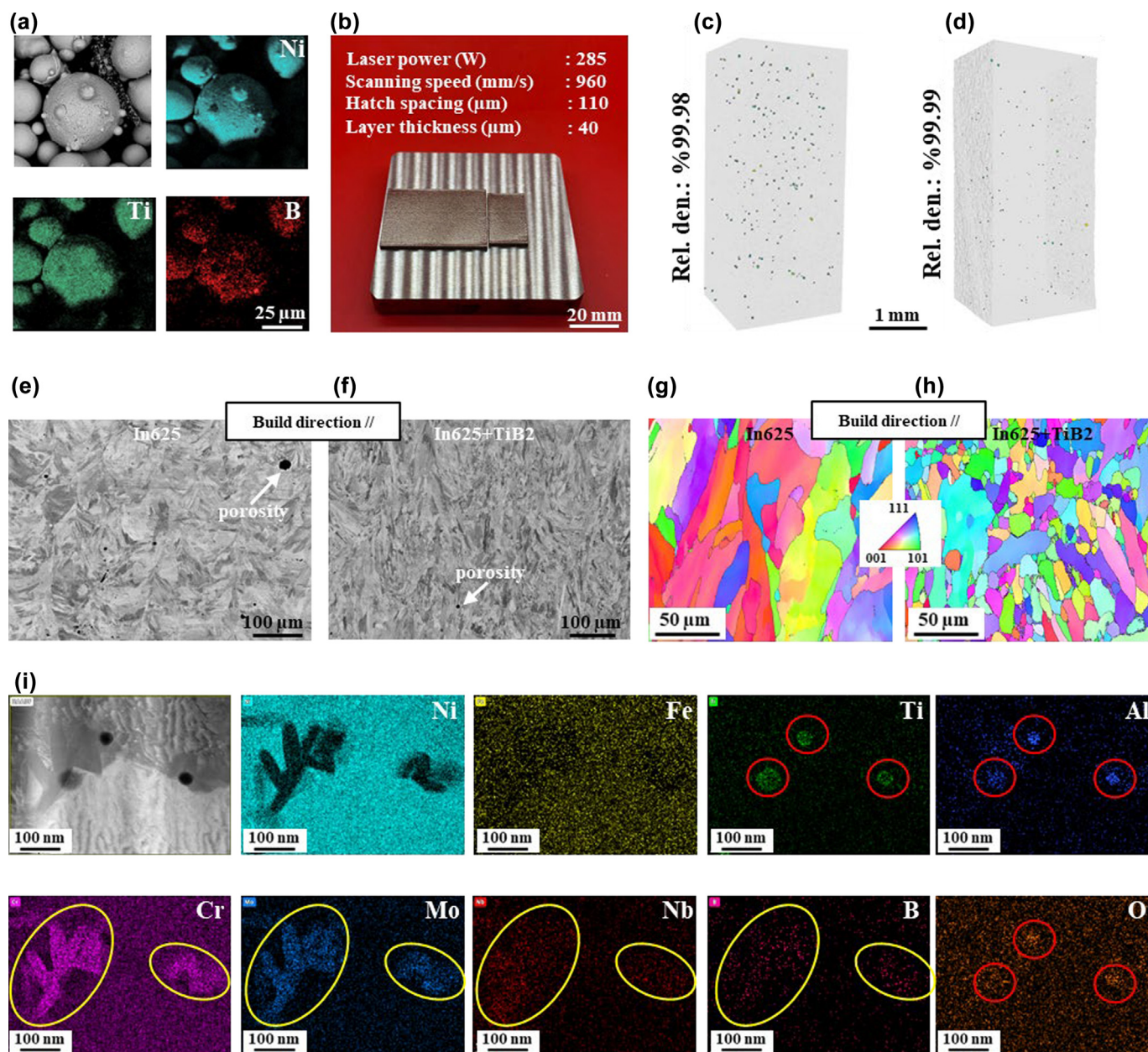
FIG. 1

(a) SEM micrographs of TiB$_2$ decorated In625 particles after blending, (b) In625 + TiB$_2$ samples fabricated by LPBF using EOS M290 system, shown prior to removal from the build plates, (c-d) 3D CT reconstructions displaying pores formed during printing of In625 and In625 + TiB$_2$ samples, (e-f) SEM images obtained from In625 and In625 + TiB$_2$, (g-h) EBSD orientation maps obtained from In625 and In625 + TiB$_2$ revealing the reduction in grain size, (i) STEM/EDX mapping micrographs obtained from In625 + TiB$_2$ shows the exchange reaction zone between Cr, Mo, Nb, Ti, and B.

ences are observable in the grain structures between In625 and In625 + TiB$_2$. The variations in grain structures become clear via the EBSD orientation maps provided in Fig. 1(g, h) and Supplementary Fig. 6. These maps reveal that the In625 + TiB$_2$ composites display a diminished and more equiaxed grain size in contrast to pure In625 and other composites.

Cross-sectional SEM images of all as-printed samples and corresponding EDX results are shown in Supplementary Fig. 7 and Supplementary Table 3, respectively. To characterize elemental interactions during LPBF, high-angle annular dark-field (HAADF)-STEM/EDX mapping in Fig. 1(i) unearths the exchange reaction zones of the following elements: Cr, Mo, Nb, Ti, and B

(indicated by yellow circles). It is important to note that the boron-rich regions overlap with Cr, Mo and Nb signals according to high-magnification STEM/EDX mapping and quantitative local EDX analysis. Boron's partition in the Cr-rich region is also accentuated via the EELS analysis in Supplementary Fig. 8, which discerns a Cr-including boride phase, and highlights TiB$_2$'s role as a potential source of boron within the LPBF'ed composite. Therefore, it could be stated that several transition metals reacted with boron (i.e., Cr, Mo and Nb) to form complex boride precipitates during LPBF. It is important to note that the decomposition kinetics of TiB$_2$ could change with varying process conditions such as laser power, scanning speed, and hatch spacing, as these

parameters determine the local temperature trajectories during LPBF. Therefore, it is worthwhile to study the effect of LPBF process parameters on the formation and distribution of secondary phases in In625 + TiB$_2$ and their relevant mechanical properties. There are also spherical dark nano precipitates, as indicated by red circles, adjacent to the boron-rich regions. These spherical precipitates are Ti-Al based oxides, as confirmed via EDX analysis (Supplementary Table 4) taken from Area 3 of Supplementary Fig. 8. The oxide particles also show higher concentrations of Nb (10.81 wt%) indicating the partition of Nb in the oxide-particles.

In the examination of the tensile stress–strain behavior of In625 and its composites, Fig. 2(a) and Table 1 shows the tensile properties of pure In625 and its composite counterparts at room temperature. Pure In625, serving as a baseline, demonstrates distinct ductility (∼35 %) compared to its composite counterparts, yet it exhibits the lowest yield strength (σ_{YS}: 841 MPa) and ultimate tensile strength values (σ_{UTS}: 1054 MPa). Among all composites fabricated in this study, In625 + TiB$_2$ notably stands out, achieving the highest σ_{UTS} value of approximately 1650 MPa, but with a low ductility (∼7%). On the other hand, In625 + ZrC shows the lowest strength-ductility pair. This could be attributed to the presence of cracks in the microstructure, as shown in Supplementary Figure 9. The cracks show strong Zr and O signals, indicating the decomposition of ZrC followed by the oxidation of Zr during LPBF. Consequently, these cracks might have formed due to oxide formation, serving as sites for crack propagation and contributing to a lower strength-ductility pair. However, no trace of crack formation was observed in the other composite specimens except the one doped with ZrC. It is noteworthy that the In625 + TiB$_2$ composite, when evaluated in terms of both σ_{YS} and σ_{UTS}, resides in a region that signifies superior room-temperature strength. SEM images taken from the fractured surfaces of pure In625 and In625 + TiB$_2$ are shown in Supplementary Figure 10. These images depict a higher density of dimples (highlighted in yellow rectangles) on the fracture surface of pure In625 compared to In625 + TiB$_2$, which also shows cleavage regions (highlighted by green rectangles). This aligns with the tensile elongation of In625 + TiB$_2$ being remarkably lower than that of pure In625 [33–35]. Shifting the focus to Fig. 2(b) and (c), a comprehensive comparison between our In625 + TiB$_2$ and findings from the existing literature is illustrated. The data points are dispersed over a range of σ_{YS} and σ_{UTS}, offering a high-level view of where the strength of In625 + TiB$_2$ from this investigation stands in relation to previous studies on the tensile performance of several Inconel alloys (i.e., In718 and In939) [24,36–42].

After evaluation of the room-temperature tensile performance of the samples, high-temperature tensile tests were performed. Representative stress–strain curves of pure In625 and other MMCs at 800 °C are depicted in Fig. 3(a), and the mechanical properties are summarized in Table 2. The experimental findings demonstrate that the MMC comprising In625 + TiB$_2$ exhibits superior tensile properties at 800 °C. In particular, In625 + TiB$_2$ displays significant enhancements of 56 %, 68 %, and 164 % in yield strength, ultimate tensile strength, and ductility, respectively, compared to pure In625 alloy. The Ashby map comparing the strength-ductility pair of In625 + TiB$_2$ with various alloys
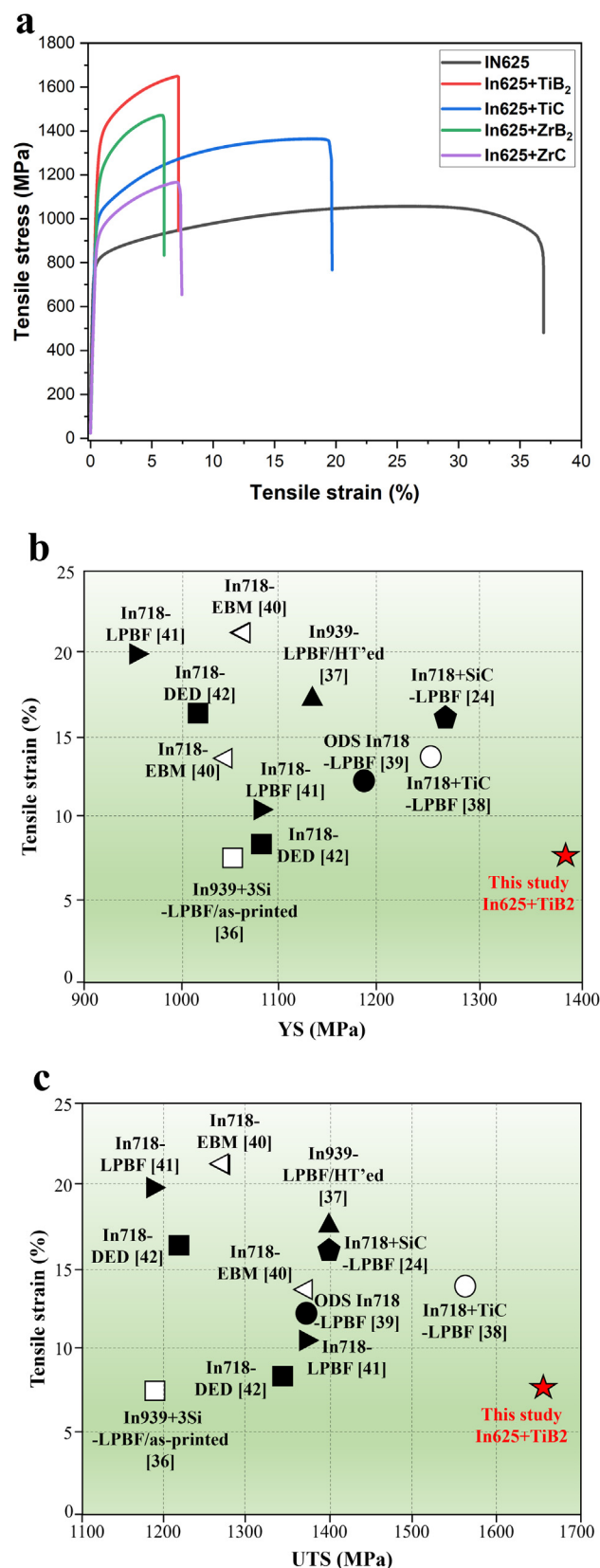
FIG. 2

Tensile stress–strain curves for In625 and its composites at (a) room temperature, and the comparative performances of various materials in terms of σ_{YS} and σ_{UTS} vs. tensile strain are shown in (b) and (c), respectively, with emphasis on the superior tensile strength of the In625 + TiB$_2$ composite fabricated in this study.

TABLE 1

Tensile properties of pure In625 and MMCs at room temperature.

Sample	σ_{YS} (MPa)	σ_{UTS} (MPa)	Elongation (%)
In625	841	1054	36.9
In625 + TiB$_2$	1386	1649	7.2
In625 + TiC	1093	1364	19.7
In625 + ZrB$_2$	1297	1471	6
In625 + ZrC	998	1165	7.5
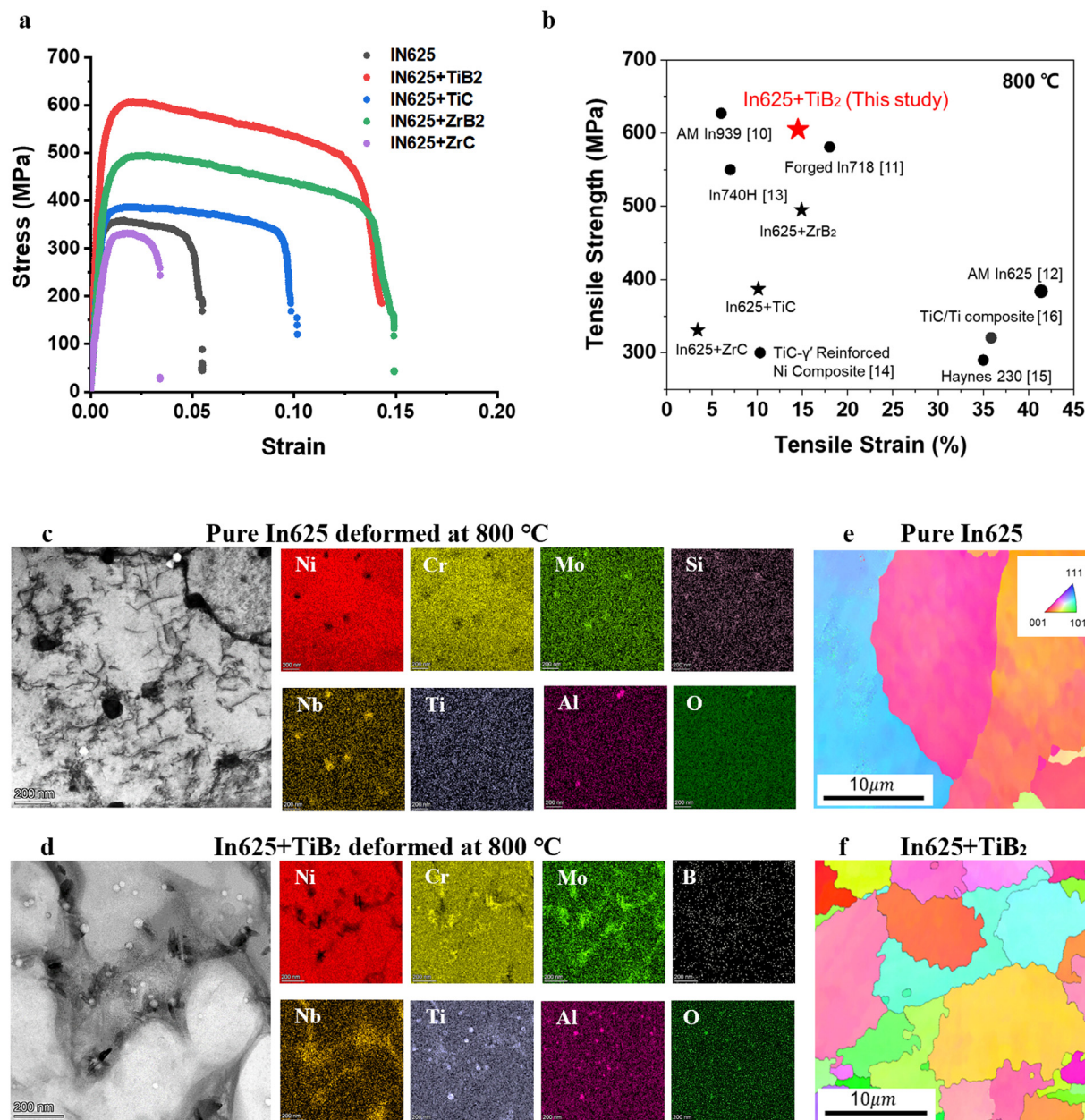
FIG. 3

(a) Stress–strain curves of pure In625 and MMCs at 800 °C; (b) Comparison of the strength-ductility pair at 800 °C: of In625 + TiB$_2$ vs. other additively manufactured (AM) and conventional alloys in the literature; (c) BF-TEM image and STEM-EDS map of deformed In625 and (d) In625 + TiB$_2$; (e) Characteristics of grain boundaries in pure In625 and (f) In625 + TiB$_2$ as confirmed through IPF maps.

RESEARCH (LIGHT BLUE)

TABLE 2

Tensile properties of pure In625 and MMCs at 800 °C.

Sample	σ_{YS} (MPa)	σ_{UTS} (MPa)	Elongation (%)
In625	332	358	5.4
In625 + TiB$_2$	520	605	14.3
In625 + TiC	362	387	10.1
In625 + ZrB$_2$	435	495	14.9
In625 + ZrC	313	331	3.4

from the literature [43–49] are shown in Fig. 3(b), where the excellent combination of strength and ductility of In625 + TiB$_2$ can be observed. Particularly, when compared to AM In939 and forged In718, it can be seen that In625 + TiB$_2$ possesses a similar or superior strength-ductility pair at 800 °C. This result implies that the MMC of In625 + TiB$_2$ presented in this study has the potential to extend the application limits of traditional In625 alloy. The superior high-temperature strength observed in the In625 + TiB$_2$ MMC can be attributed to its microstructural characteristics. TEM results, as shown in Fig. 3(c) and (d), reveal the microstructural features of deformed In625 and In625 + TiB$_2$ at 800 °C. A comparative analysis with pure In625 highlights the presence of a dispersed array of fine spherical particles within In625 + TiB$_2$, accompanied by intermetallic compounds. Utilizing STEM-EDS mapping, the fine spherical particles have been identified as Ti-Al oxide nanoparticles, and the surrounding intermetallic compounds have been confirmed to be (Cr, Mo)-based borides. The presence of stable Ti-Al oxide nanoparticles in high-temperature environments, along with the formation of (Cr, Mo)-based borides around them, effectively impedes dislocation movement at room temperature as well as at elevated temperatures [45,50,51]. To achieve a more comprehensive understanding of the observed microstructural features, the calculation of the phase diagram (CALPHAD) was conducted using ThermoCalc based on the TTNI8 database. The CALPHAD results presented in Supplementary Fig. 11 and Table 3 show the calculated secondary phase fraction at 800 °C for both pure In625 and TiB$_2$-doped In625. The In625 + TiB$_2$ result indicates that the gamma prime (γ') phase and the M$_3$B$_2$ phase are predominant. M$_3$B$_2$ phase is considered to be the (Cr, Mo)-based boride phase [52,53], as observed in Fig. 3(d). However, it is noteworthy that the Ni$_3$(Ti, Al) γ' phase was not readily apparent in the TEM results of the deformed In625 + TiB$_2$ sample. Previous investigations on precipitate phase formation in nickel-based superalloys have reported that an increased (Al + Ti)/Nb ratio promotes the formation of the γ' phase [54,55]. It is presumed that these findings have been integrated into the TTNI8 database, thereby indicating a substantial presence of the γ' phase in the MMC of

In625 + TiB$_2$. However, our experimental observation suggests that during the L-PBF process to fabricate In625 + TiB$_2$ MMC, Ti and Al, the primary elements of the γ' phase, are more inclined to form Ti-Al oxide nanoparticles rather than the γ' phase. Previous studies have revealed the mechanism underlying the formation of oxide nanoparticles during the LPBF process. In the gas or liquid atomization process employed to produce powders for LPBF, a thin oxide layer develops on the powder's surface [56]. This oxide layer is susceptible to fragmentation and melting by high-energy laser or electron beam during the fabrication process, releasing oxygen into the melt pool [57,58]. The released oxygen can then react with alloy elements in the melt pool, such as Ti, Al, Si and Mn, which are known for their high affinity to oxygen [57,58]. This phenomenon is likely to result in the formation of nanosized oxide particles during the rapid solidification process. Considering the characteristics of In625 + TiB$_2$ MMC powders, decorated with nanosized TiB$_2$ particles on their surface, the formation of oxide nanoparticles is expected to be further facilitated. The unique microstructural features observed in TiB$_2$-fortified In625 can serve as the basis for various strengthening mechanisms that enhance the material's strength. The proposed model for strengthening mechanisms is discussed in detail in the supplementary information (Supplementary Fig.14, Supplementary Table 5 and 6). In625 + TiB$_2$ exhibits exceptional ductility at 800 °C compared to other MMCs of this study (Fig. 3(a)). On the fracture surfaces of In625 + ZrB$_2$ and In625 + TiB$_2$, which experienced significant plastic deformation, ductile fracture characteristics, such as the formation of voids and dimples, were clearly evident (Supplementary Fig. 12). The outstanding ductility of In625 + TiB$_2$ at 800 °C can be linked to the distinct characteristics of its grain boundaries, as confirmed by the EBSD analysis. Fig. 3(e) and (f) illustrate the differences in grain boundary features between pure In625 and In625 + TiB$_2$. In contrast to pure In625, the grain boundaries of In625 + TiB$_2$ display more pronounced serrated characteristics and finer grain size. Given that the inverse pole figure (IPF) maps were captured with a consistent step size (0.03 μm), the marked difference in grain boundary characteristics between the pure

TABLE 3

Relative secondary phase fraction (vol%) at 800 °C from CALPHAD results.

Sample	γ'	M$_3$B$_2$	δ	σ	M$_{23}$C$_6$	M$_6$C
In625	—	—	7.064	2.426	0.949	2.043
In625 + TiB$_2$	8.224	8.187	5.827	—	2.290	—

In625 and In625 + TiB$_2$ is clearly discernible. The presence of serrated grain boundaries is known to have a significant impact on the mechanical properties of nickel-based superalloys by impeding crack propagation along grain boundaries [59–61]. Specifically, it is postulated that voids and cavities along these serrated grain boundaries resist easy percolation, thereby impeding the formation of a continuous crack path [60,61]. This effect is particularly dominant in environments characterized by high temperatures and low strain rates, where failure mechanisms are controlled by diffusional phenomena at grain boundaries [60]. Thus, the enhanced ductility of In625 + TiB$_2$ over undoped In625 at 800 °C is attributed to the presence of serrated grain boundary features.

The question that arises is the mechanism behind the formation of serrated grain boundaries in TiB$_2$-doped In625. Numerous studies have been dedicated to elucidating the formation mechanism of serrated grain boundaries in nickel-based superalloys. It is generally suggested that the development of serrated grain boundaries results from the interaction between the precipitates or solutes at the grain boundaries and the movement of these boundaries [62,63]. Moreover, recent investigation has demonstrated that the solution treatment temperature and slow cooling rates that lead to strong elemental segregation at grain boundaries are critical factors influencing the formation of serrated grain boundaries [59]. However, given that In625 + TiB$_2$ does not undergo solution treatment, it is anticipated that an alternative mechanism must have played a role. It has also been reported that such characteristics of grain boundaries may result from differences in lattice strain energy around the grain boundaries, induced by the diffusion and segregation of alloying elements, even in the absence of precipitates at grain boundaries [64]. Specifically, discontinuous segregation of Cr, C and B along the grain boundaries has been suggested to contribute to the formation of serrated grain boundaries [60,64,65]. Based on previous findings, it is reasonable to infer that the addition of B likely contributed to the development of serrated grain boundary characteristics in In625 + TiB$_2$. To investigate the influence of B atoms on the microstructure from an atomic perspective, in-house Monte-Carlo-molecular-dynamics simulations were conducted. The calculations were executed using version 5.0.0 of the core neural network preferred potential (PFP) [66,67] on Matlantis. The release of the PFP v5 included verified accuracy against density functional theory calculations [68]. All simulations were performed on a defect-free lattice at 800 °C. The resulting $4 \times 4 \times 4$ FCC super cell structures of the + ZrC and + TiB$_2$ composites are depicted in Supplementary Figure 13. It is important to note that C only occupied the octahedral interstitial sites, while B atoms are found in both octahedral and tetrahedral interstitial sites of the FCC lattice. This gave rise to the formation of more complex B-based phases with surrounding metal atoms and suggests that B would have greater mobility than C in the In625 lattice. Increased B mobility implies that B-based phases would be more uniformly distributed throughout the In625 matrix, leading to more significant changes in the serrated GBs of the In625 + TiB$_2$ sample. Coupling these simulated observations with the experimentally observed serrated grain boundaries of the + TiB$_2$ sample, it is apparent that B has a profound effect on the microstructural evolution of the system. The

ability of B to occupy multiple interstitial sites suggests that it can significantly influence GB characteristics, promoting the formation of serrated GBs. The following section will offer further discussions on the superiority of In625 + TiB$_2$ compared to other MMCs, with a specific focus on thermal creep behavior.

The creep test results for all specimens (In625, In625 + ZrC, In625 + TiC, In625 + ZrB$_2$, In625 + TiB$_2$) are shown in Fig. 4(a). TiB$_2$ and ZrB$_2$ doped In625 specimens consistently show increased creep strain, followed by TiC and ZrC doped In625 and pure In625. Notably, In625 + ZrB$_2$ shows the highest creep strain at 57.2 %, and In625 with the lowest creep strain at 8 %. In terms of creep rupture time, In625 + TiB$_2$ demonstrates the longest duration at 547 h, while In625 exhibits the shortest duration at 32 h. Pure In625 exhibits the highest steady-state creep rate (Table 4). Consistently low steady-state creep rates are observed for Ti-containing In625 composites, and Zr-containing composites exhibit slightly increased, yet similar steady-state creep rates. Looking at the creep results from the perspective of material functionality, although In625 + ZrB$_2$ exhibits the highest creep strain (i.e., 57.2 % of creep deformation), the material shows ∼2.6 times lower time to rupture during creep compared to that of In625 + TiB$_2$. Fig. 4(b) compares the obtained creep rupture strain with the creep rupture strain of wrought In625 and AM In625 from previous studies [30–32]. Pure In625 exhibits a similar creep strain of ∼8 % with In625 specimens manufactured by hot isostatic pressing [30,31]. The AM composite specimens in this study consistently exhibit increased rupture strains compared to AM In625, with In625 + ZrB$_2$ specimens in this study exhibiting a similar rupture strain to that of wrought In625 specimens. Fig. 4(c) compares the time to rupture for the AM specimens in this study with those of previously reported wrought In625 specimens. Interestingly, the time to rupture for the In625 + TiB$_2$ specimen exceeds that of wrought In625 by nearly an order of magnitude.

CALPHAD simulations help rationalize the observed creep behavior as well. Fig. 4(d) shows the temperature-dependent equilibrium phases for In625 and In625 + TiB$_2$, assuming complete dissolution of TiB$_2$. Around 800 °C, In625 is calculated to form topologically close-packed (TCP) phases (primarily delta (δ)- and sigma (σ) precipitates), which are known to undermine high-temperature creep performance [69]. Supplementary Fig. 15 shows that the creep-deformed In625 specimen contains needle-like phases (highlighted in white circles). These precipitates are enriched with Ni and Nb, confirming the formation of δ-phase in the undoped specimen. On the other hand, σ-phase is not observed during SEM characterizations of creep-deformed In625 specimen. δ- and σ-phases are also observed in CALPHAD simulations of In625 + ZrC, which exhibits the lowest ductility during high-temperature tensile tests. In TiB$_2$ and ZrB$_2$ doped composites and In625 + TiC composites, the σ-phase is not observed in the phase diagram, which could be one of the reasons behind the better high-temperature tensile and creep properties in these specimens. Notably, (CrMo)$_3$B$_2$ borides form in the In625 + TiB$_2$ specimen according to the phase diagram. It is known that adding Cr and Mo to Ni often results in the nucleation of σ-phases (Ni-Cr-Mo) at high T (620 °C < T < 900 °C) [69]. When boron is introduced, we observe from the CALPHAD calculations that Cr and Mo atoms form (CrMo)$_3$B$_2$ phases in

RESEARCH (LIGHT BLUE)
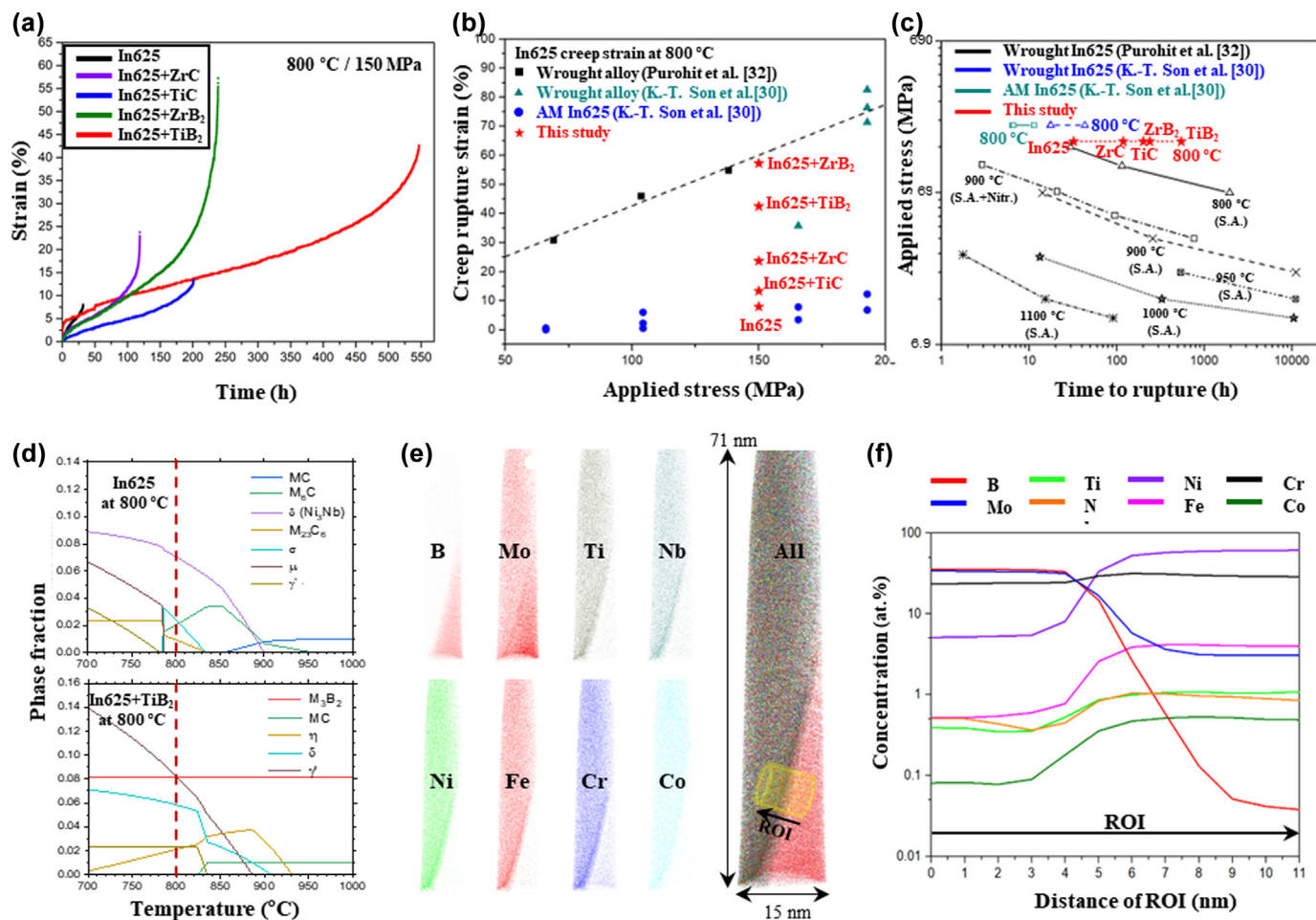
FIG. 4

(a) Creep test results for specimens of In625, In625 + ZrC, In625 + TiC, In625 + ZrB$_2$, In625 + TiB$_2$ under conditions of 800 °C and 150 MPa, (b) comparative analysis of creep rupture strain vs applied stress with other creep test results based on applied stress, (c) comparative analysis of applied stress vs. time to rupture with other creep test results (S.A. refers to solution annealing), (d) Temperature-dependent phase fraction graphs for In625 and In625 + TiB$_2$ calculated using ThermoCalc, (e) atom probe tomography data on the In625 + TiB$_2$ after creeping at a stress of 150 MPa at a temperature of 800 °C, and (f) atomic concentration graph from APT data within the region of interest (ROI).

TABLE 4

Secondary creep strain rate of pure In625 and MMCs at 800 °C and 150 MPa.

Sample	Creep strain rate (1/s)
In625	3.57×10^{-7}
In625 + TiB$_2$	1.02×10^{-7}
In625 + TiC	9.98×10^{-8}
In625 + ZrB$_2$	2.68×10^{-7}
In625 + ZrC	2.25×10^{-7}

700–1000 °C ranges instead, effectively avoiding σ-phases. Furthermore, TEM/EDX mappings obtained from creep-deformed In625 + TiB$_2$ specimens also confirm that there is no δ- and σ-phase formed in the TiB$_2$ doped composite (Supplementary Fig. 16). The results indicate a substantial partitioning of Nb to (Cr,Mo)-boride and Ti-Al oxide nanoparticles formation during LPBF (Supplementary Fig. 8 and Supplementary Table 4), which could have suppressed the precipitation of Nb-rich δ-phase in

the In625 + TiB$_2$ specimen during creep test (Supplementary Fig. 16(a) and (b)).

APT of the creep-deformed In625 + TiB$_2$ specimen near the grain boundary region reveals that (Cr, Mo)-boride phases, which formed during LPBF, remained near grain boundaries during creep tests (Fig. 4(e)). A cylinder-shaped region of interest (ROI) was set before and after the composition boundary (Fig. 4(f)) and shows that B concentration sharply increases to 35 % at the grain boundary from 0.04 % beyond the boundary. Mo also exhibits a concentration of 34 % at the grain boundary, compared to 3 % in the bulk region. The approximate composition of the boride from the compositional map corresponds to Mo$_2$-CrB$_2$, matching well with the CALPHAD results.

Conclusions

A range of In625-based metal matrix composites (MMCs), specifically those incorporating TiB$_2$, TiC, ZrB$_2$, and ZrC, were synthesized utilizing the LPBF method. The incorporation of these dopants led to notable microstructural alterations, which in turn

significantly enhanced the mechanical performance of the In625 + TiB$_2$ MMCs at both ambient and elevated temperatures, particularly in terms of tensile strength and creep resistance, when compared to the baseline In625 material and other MMC variants. The observed exceptional increase in mechanical strength for the TiB$_2$-fortified MMC is attributed to synergistic strengthening effects, including grain refinement, solute strengthening, and dispersion hardening mechanisms. Specifically, at ambient conditions, the In625 composite fortified with TiB$_2$ demonstrated superior yield strength (σ_{YS}) and ultimate tensile strength (σ_{UTS}) of 1386 MPa and 1649 MPa, respectively, albeit at the expense of ductility, which was measured to be 7.2 % tensile elongation. When subjected to tensile tests at 800 °C, however, the In625 + TiB$_2$ composite exhibited a 70 % improvement in σ_{UTS} and a threefold increase in elongation compared to unmodified In625. Furthermore, the TiB$_2$-fortified composite showed a remarkable enhancement in creep resistance at 800 °C under a stress of 150 MPa, with the time to creep rupture extending beyond 15 times that of pure In625. These findings indicate that the development of TiB$_2$-doped In625 MMCs could substantially elevate the material's performance in high-temperature applications, potentially expanding its use in high-demand settings such as in nuclear fusion reactors and gas turbines. Consequently, this study's demonstration of a scalable fabrication technique for In625 + TiB$_2$ MMCs presents a promising avenue for the production of components designed for use in challenging environmental conditions.

CRediT authorship contribution statement

Emre Tekoglu: Writing – review & editing, Writing – original draft, Software, Methodology, Investigation, Formal analysis, Data curation. **Jong-Soo Bae:** Writing – review & editing, Writing – original draft, Investigation, Formal analysis, Data curation. **Ho-A Kim:** Writing – original draft, Investigation, Formal analysis, Data curation. **Kwang-Hyeok Lim:** Writing – review & editing, Investigation, Formal analysis. **Jian Liu:** Writing – review & editing, Formal analysis, Data curation. **Tyler D. Doleẑal:** Writing – review & editing, Formal analysis, Data curation. **So Yeon Kim:** Writing – review & editing, Formal analysis, Data curation. **Mohammed A. Alrizqi:** Writing – review & editing, Formal analysis. **Aubrey Penn:** Writing – review & editing, Formal analysis. **Wen Chen:** Writing – review & editing, Supervision. **A. John Hart:** Writing – review & editing, Supervision. **Joo-Hee Kang:** Writing – review & editing, Formal analysis. **Chang-Seok Oh:** Writing – review & editing, Investigation, Formal analysis. **Jiwon Park:** Writing – review & editing, Formal analysis. **Fan Sun:** Writing – review & editing, Formal analysis, Data curation. **Sangtae Kim:** Writing – review & editing, Writing – original draft, Visualization, Validation, Supervision, Project administration, Methodology, Investigation, Conceptualization. **Gi-Dong Sim:** Writing – review & editing, Visualization, Validation, Supervision, Resources, Project administration, Methodology, Investigation, Funding acquisition, Conceptualization. **Ju Li:** Writing – review & editing, Visualization, Validation, Supervision, Resources, Project administration, Methodology, Investigation, Funding acquisition, Conceptualization.

Data availability

Data will be made available on request.

Declaration of competing interest

The authors declare that they have no known competing financial interests or personal relationships that could have appeared to influence the work reported in this paper.

Author contributions statement

E.T. and J.S.B. analyzed the results, characterized the materials, and wrote; H.K. performed creep tests, characterized crept sample, and wrote; K.H.L. performed HT tensile tests and fracture surface analysis; J. Liu performed RT tensile tests; T.D.D. developed the hybrid Monte-Carlo-molecular-dynamics routine and provided preliminary atomistic insights; S.Y.K. carried out TEM sample preparation; M.A. supported the materials characterizations study; A.P. performed TEM studies; W.C. oversaw the study and provided editing; A-.J.H. oversaw the study and provided editing; J.H.K. oversaw the study and provided editing; C.S.O. performed thermodynamic calculations; J.W.P. oversaw the study and provided editing; F.S. performed TEM studies on tensile deformed specimens and provided editing; S.K., G.D.S. and J. Li conceived the project idea, oversaw the study and provided editing.

Declaration of generative AI and AI-assisted technologies in the writing process

During the preparation of introduction EMRE TEKOGLU used ChatGPT (GPT-4, OpenAI) in order to improve the readability. After using this tool/service, all of the authors reviewed and edited the content as needed and take full responsibility for the content of the publication.

Appendix A. Supplementary material

Supplementary material to this article can be found online at https://doi.org/10.1016/j.mattod.2024.09.006.

References

[1] J. Ren et al., Nature 608 (2022) 62–68. https://doi.org/10.1038/s41586-022-04914-8.

[2] E.J. Pickering et al., Entropy 23 (2021) . https://doi.org/10.3390/e23010098.

[3] B. Li et al., Powder Technol. 360 (2020) 509–521. https://doi.org/10.1016/j.powtec.2019.10.068.

[4] C. Haase et al., Mater. Sci. Eng. A 688 (2017) 180–189. https://doi.org/10.1016/j.msea.2017.01.099.

RESEARCH (LIGHT BLUE)

[5] W. Cheng et al., J. Mater. Res. Technol. 24 (2023) 7497–7524. https://doi.org/10.1016/j.jmrt.2023.05.037.

[6] G. Marinelli et al., Sci. Technol. Weld. Join. 24 (2019) 495–503. https://doi.org/10.1080/13621718.2019.1586162.

[7] N.R. Philips, M. Carl, N.J. Cunningham, Metall. Mater. Trans. A 51 (2020) 3299–3310. https://doi.org/10.1007/s11661-020-05803-3.

[8] P.D. Awasthi et al., Mater. Sci. Eng. A 831 (2022) 142183. https://doi.org/10.1016/j.msea.2021.142183.

[9] D.H. Cook et al., Science 384 (2024) (1979) 178–184. https://doi.org/10.1126/science.adn2428.

[10] E.O. Olakanmi, R.F. Cochrane, K.W. Dalgarno, Prog. Mater Sci. 74 (2015) 401–477. https://doi.org/10.1016/j.pmatsci.2015.03.002.

[11] M.-Y. Shen et al., J. Alloys Compd. 734 (2018) 188–195. https://doi.org/10.1016/j.jallcom.2017.10.280.

[12] W. Zhang et al., Corros. Sci. 205 (2022) 110422. https://doi.org/10.1016/j.corsci.2022.110422.

[13] J. Feng et al., Corros. Sci. 197 (2022) 110097. https://doi.org/10.1016/j.corsci.2022.110097.

[14] H. Liu et al., Corros. Sci. 193 (2021) 109869. https://doi.org/10.1016/j.corsci.2021.109869.

[15] Y. Su et al., J. Mater. Sci. 56 (2021) 16745–16761. https://doi.org/10.1007/s10853-021-06357-4.

[16] Z. Dai et al., Mater. Sci. Eng. A 854 (2022) 143626. https://doi.org/10.1016/j.msea.2022.143626.

[17] B. Zhang et al., Mater. Des. 111 (2016) 70–79. https://doi.org/10.1016/j.matdes.2016.08.078.

[18] V. Promakhov et al., Metals (Basel) 9 (2019) . https://doi.org/10.3390/met9020141.

[19] B. Zhang et al., Opt. Laser Technol. 80 (2016) 186–195. https://doi.org/10.1016/j.optlastec.2016.01.010.

[20] M. Karbalaei Akbari, H.R. Baharvandi, O. Mirzaee, Compos. B Eng. 55 (2013) 426–432. https://doi.org/10.1016/j.compositesb.2013.07.008.

[21] Q. Hu, H. Zhao, F. Li, Mater. Sci. Eng. A 680 (2017) 270–277. https://doi.org/10.1016/j.msea.2016.10.090.

[22] J. Segurado, C. González, J. LLorca, Acta Mater. 51 (2003) 2355–2369. https://doi.org/10.1016/S1359-6454(03)00043-0.

[23] C. Doñate-Buendía et al., Mater. Des. 154 (2018) 360–369. https://doi.org/10.1016/j.matdes.2018.05.044.

[24] E. Tekoğlu et al., Addit. Manuf. 67 (2023) 103478. https://doi.org/10.1016/j.addma.2023.103478.

[25] E. Tekoğlu et al., Compos. B Eng. 268 (2024) 111052. https://doi.org/10.1016/j.compositesb.2023.111052.

[26] S.H. Kim et al., Sci. Rep. 7 (2017) 14359. https://doi.org/10.1038/s41598-017-14713-1.

[27] D.E. Cooper et al., J. Mater. Process. Technol. 213 (2013) 2191–2200. https://doi.org/10.1016/j.jmatprotec.2013.06.021.

[28] Y.-C. Zhang et al., Eng. Fract. Mech. 199 (2018) 327–342. https://doi.org/10.1016/j.engfracmech.2018.05.048.

[29] X. Liu et al., Mater. Sci. Eng. A 829 (2022) 142152. https://doi.org/10.1016/j.msea.2021.142152.

[30] K.-T. Son, M.E. Kassner, K.A. Lee, Adv. Eng. Mater. 22 (2020) 1900543. https://doi.org/10.1002/adem.201900543.

[31] K.-T. Son et al., Materialia (Oxf) 15 (2021) 101021. https://doi.org/10.1016/j.mtla.2021.101021.

[32] A. Purohit, W.F. Burke, Elevated temperature creep behavior of Inconel alloy 625, in: United States, 1984. https://www.osti.gov/biblio/6769534.

[33] F. Chen et al., Mater. Sci. Eng. A 625 (2015) 357–368. https://doi.org/10.1016/j.msea.2014.12.033.

[34] X. Yuan et al., J. Manuf. Process. 77 (2022) 63–74. https://doi.org/10.1016/j.jmapro.2022.03.008.

[35] J.A. Gonzalez et al., J. Mater. Process. Technol. 264 (2019) 200–210. https://doi.org/10.1016/j.jmatprotec.2018.08.031.

[36] B. Zhang et al., Addit. Manuf. 72 (2023) 103623. https://doi.org/10.1016/j.addma.2023.103623.

[37] I. Šulák et al., J. Mech. Sci. Technol. 37 (2023) 1071–1076. https://doi.org/10.1007/s12206-022-2101-7.

[38] X. Yao et al., Int. J. Precis. Eng. Manuf. 18 (2017) 1693–1701. https://doi.org/10.1007/s12541-017-0197-y.

[39] Q. Song et al., Opt. Laser Technol. 144 (2021) 107423. https://doi.org/10.1016/j.optlastec.2021.107423.

[40] M.M. Kirka et al., Mater. Sci. Eng. A 680 (2017) 338–346. https://doi.org/10.1016/j.msea.2016.10.069.

[41] D. Zhang et al., Mater. Sci. Eng. A 644 (2015) 32–40. https://doi.org/10.1016/j.msea.2015.06.021.

[42] H. Qi, M. Azer, A. Ritter, Metall. Mater. Trans. A 40 (2009) 2410–2422. https://doi.org/10.1007/s11661-009-9949-3.

[43] Y.T. Tang et al., in: Superalloys 2020, Springer International Publishing, Cham, 2020, pp. 1055–1065.

[44] M.C. Rezende et al., J. Alloys Compd. 643 (2015) S256–S259. https://doi.org/10.1016/j.jallcom.2014.12.279.

[45] M. Li et al., Mater. Sci. Eng. A 854 (2022) 143813. https://doi.org/10.1016/j.msea.2022.143813.

[46] C. Kumar, P. Kumar, Materialia (Oxf) 33 (2024) 102028. https://doi.org/10.1016/j.mtla.2024.102028.

[47] W. Hu et al., Met. Mater. Int. 27 (2021) 3003–3012. https://doi.org/10.1007/s12540-020-00615-x.

[48] K. Hrutkay, D. Kaoumi, Mater. Sci. Eng. A 599 (2014) 196–203. https://doi.org/10.1016/j.msea.2014.01.056.

[49] H.W. Wang et al., Mater. Sci. Eng. A 545 (2012) 209–213. https://doi.org/10.1016/j.msea.2012.03.037.

[50] S. Pasebani et al., Mater. Sci. Eng. A 630 (2015) 155–169. https://doi.org/10.1016/j.msea.2015.01.066.

[51] B. Reppich, Acta Mater. 46 (1998) 61–67. https://doi.org/10.1016/S1359-6454(97)00234-6.

[52] X.B. Hu et al., Sci. Rep. 4 (2014) 7367. https://doi.org/10.1038/srep07367.

[53] B. Schulz, T. Leitner, S. Primig, J. Alloys Compd. 956 (2023) 170324. https://doi.org/10.1016/j.jallcom.2023.170324.

[54] A.J. Detor et al., Metall. Mater. Trans. A 49 (2018) 708–717. https://doi.org/10.1007/s11661-017-4356-7.

[55] L.-J. Yu, E.A. Marquis, J. Alloy. Compd. 811 (2019) 151916. https://doi.org/10.1016/j.jallcom.2019.151916.

[56] Y. Sun, R.J. Hebert, M. Aindow, Mater. Des. 140 (2018) 153–162. https://doi.org/10.1016/j.matdes.2017.11.063.

[57] D. Kong et al., Addit. Manuf. 38 (2021) 101804. https://doi.org/10.1016/j.addma.2020.101804.

[58] Y.M. Wang et al., Nat. Mater. 17 (2018) 63–71. https://doi.org/10.1038/nmat5021.

[59] Y.T. Tang et al., Acta Mater. 181 (2019) 352–366. https://doi.org/10.1016/j.actamat.2019.09.037.

[60] P. Kontis et al., Acta Mater. 124 (2017) 489–500. https://doi.org/10.1016/j.actamat.2016.11.009.

[61] H.L. Danflou, M. Marty, A. Walder, Superalloys (1992) 63–72. https://api.semanticscholar.org/CorpusID:51787288.

[62] M.F. Henry et al., Metall. Trans. A 24 (1993) 1733–1743. https://doi.org/10.1007/BF02657848.

[63] A.K. Koul, G.H. Gessinger, Acta Metall. 31 (1983) 1061–1069. https://doi.org/10.1016/0001-6160(83)90202-X.

[64] H.U. Hong et al., Philos. Mag. 92 (2012) 2809–2825. https://doi.org/10.1080/14786435.2012.676212.

[65] D. Blavette et al., Acta Mater. 44 (1996) 4995–5005. https://doi.org/10.1016/S1359-6454(96)00087-0.

[66] S. Takamoto et al., Nat. Commun. 13 (2022) 2991. https://doi.org/10.1038/s41467-022-30687-9.

[67] S. Takamoto et al., J. Materiomics 9 (2023) 447–454. https://doi.org/10.1016/j.jmat.2022.12.007.

[68] MATLANTIS, PFP validation for public V5.0.0, (2021).

[69] Ö. Özgün et al., J. Alloys Compd. 546 (2013) 192–207. https://doi.org/10.1016/j.jallcom.2012.08.069.